Influence of Laser-Interaction Parameters on the Mechanical Properties of Limestone Rock for Geothermal Resource Exploration

Antash K Sinha and Shrikrishna N Joshi*

Department of Mechanical Engineering, Indian Institute of Technology Guwahati, Guwahati – 781039, Assam, India
*Corresponding author's e-mail: snj@iitg.ac.in

Laser-assisted rock drilling presents a viable pathway to address limitations in conventional drilling methods, such as high bit wear and reduced efficiency in hard formations. This study investigates the softening behavior of limestone under continuous wave CO₂ laser irradiation by varying key processing parameters: laser power (126-162 W), stand-off distance (6-8 mm), scanning speed (30-50 mm/s), and scan-line interval (0.1-0.3 mm). A general full factorial design comprising 81 experimental runs was adopted, with Rockwell hardness (HRA) as the primary metric for evaluating the laser-induced weakening. Results revealed that HRA decreased with higher laser power, slower scanning speeds, and narrower scan intervals, highlighting enhanced thermal absorption and microstructural damage. Samples irradiated at shorter stand-off distances exhibited greater softening due to higher energy density. Box plot analyses confirmed parametric sensitivity, with lowest median HRA values often recorded at 0.1 mm intervals and 30 mm/s scan speed. Scanning electron microscopy further supports the trend showing grain boundary decohesion, localized melting, and disaggregated micro-textures in irradiated samples, contrasting with the dense, crack-free microstructure of the pristine limestone. The study establishes Rockwell hardness as an effective indicator of laser-induced damage and offers insights for optimizing laser parameters in Combined thermo-mechanical drilling (CTMD) applications.

DOI: 10.2961/jlmn.2025.03.2010

Keywords: laser-rock drilling, limestone, parametric analysis, Rockwell hardness, heat-affected zone,

microstructure

1. Introduction

Laser-assisted rock processing is emerging as a promising approach to overcome limitations associated with conventional mechanical drilling methods, especially in applications involving hard or heterogeneous lithologies. Traditional drill bits such as polycrystalline diamond compact (PDC) and tungsten carbide (TC) often face challenges such as rapid wear, low penetration rates, reduced efficiency, and high operational costs when deployed in deep, high-strength rock formations [1-3]. To enhance performance and minimize wear, recent advancements in Combined Thermo-Mechanical Drilling (CTMD) technologies have integrated non-contact thermal sources-most notably lasers-with conventional mechanical systems to induce pre-weakening of the rock through softening, spallation, melting, and vaporization [4-5]. All the thermal spallation-based drilling approaches have emerged as propitious in softening the rock, making it economical for the conventional bits to penetrate further [6].

Among the thermal energy sources, high-power continuous wave (CW) CO₂ lasers offer notable advantages for the CTMD applications. Their ability to deliver sustained, localized heating makes them well-suited for gradual energy deposition in geological materials, enabling controlled thermal softening without excessive fragmentation [7-8]. Unlike pulsed lasers – which may cause abrupt energy surges and localized spallation – the continuous nature of CW lasers facilitates steady crack evolution and microstructural modification, which is beneficial for repeatable hardness

measurements in brittle rock materials. Assessment of potential for laser-based rock interactions started in the early 1960s and gained traction since 1997 through collaborative studies by Argonne National Laboratory, Gas Technology Institute, Parker Geoscience Consulting Firm, and Colorado School of Mines [9-11]. Since then, numerous investigations have been conducted on vital geothermal rocks such as granite [12-13], shale [14-15], sandstone [16-17], basalt [18], and limestone [19-20]. Based on these investigations, it is found that laser-rock interaction involves complex thermal and mechanical phenomena such as thermal spallation, microcracking, and structural degradation. The interaction is governed by factors such as laser power, exposure time, beam diameter, and stand-off distance. A proper combination of these parameters is vital in determining the energy deposited at the workpiece surface, material removal, penetration depth, energy consumption, and efficacy of the process.

Laser-material interaction varies significantly between metals and rocks due to fundamental differences in their physical and thermal properties. Metals are typically homogeneous, crystalline, and highly conductive, exhibiting high reflectivity and low absorptivity at common laser wavelengths (e.g., CO₂ and Nd: YAG). Consequently, laser energy on metals is primarily absorbed at the surface, inducing melting and vaporization, which facilitates processes like cutting, welding, or additive manufacturing. In contrast, rocks are heterogeneous, porous, and composed of multiple mineral phases with inherently low thermal conductivity and

higher absorptivity. These characteristics lead to deeper thermal penetration and non-uniform heating, resulting in brittle fracture, thermal spallation, and crack propagation as dominant rock mechanisms. Furthermore, the heat-affected zone in rocks is broader and less predictable due to their anisotropic and inhomogeneous structure. Therefore, unlike the predictable and controlled thermal response of metals, laserrock interaction is governed by complex thermomechanical phenomena requiring distinct modeling approaches and process parameters. Laser-rock interaction occurs through the mechanisms of spallation, melting, vaporization, and sublimation [21-22]. The stages observed during this process are: localized heating at the surface, pores and voids coalescence, voids enlargement, cracking, crack branching, and ultimately fracturing of the rocks. These aspects require ardent investigation for response behavior with respect to laser processing parameters and rock properties [23].

Hardness is a key parameter influencing the physio-mechanical properties of rock during the laser-rock interaction, directly affecting the rock's excavability and breakage characteristics [24]. It provides an indirect measure of the rock's breaking strength and is often incorporated into empirical relations for predicting drilling performance [25]. A reduction in surface hardness corresponds to lower resistance against penetration, whether by a laser beam or a mechanical bit, which can significantly enhance cutting or drilling rates. In Combined Thermo-Mechanical Drilling (CTMD), laser-induced softening preconditions the rock, facilitating more efficient mechanical fragmentation. Various hardness testing methods, including Schreiner [25], Leeb [26], Schmidt, Brinell [27], and Rockwell [20], have been employed in assessing rock excavability and drillability across different excavation processes. Among them, Mohs [28] and Rebound hardness [29] tests are widely used in drilling studies; however, their applicability at the laboratory scale is limited due to challenges in achieving high-accuracy results, robustness, and repeatability, particularly when assessing small, localized zones. In literature, rock hardness evaluation techniques are generally classified as static or dynamic methods, both serving as cost-effective alternatives to destructive testing methods such as unconfined compressive strength and Brazilian tensile testing. Dynamic methods are more suited to field applications, whereas static methods are preferred for controlled laboratory evaluations. Despite extensive research on rock hardness, studies specifically employing hardness-based analysis for laser-rock interaction remain scarce, with most limited to nanoindentation-based evaluations. In this context, Rockwell hardness (HRA) offers a quantitative, repeatable, and highly sensitive measure of laser-induced mechanical property changes. Its ability to detect subtle thermal and structural softening in confined laseraffected regions enables effective monitoring of progressive weakening trends, demonstrating strong potential for laboratory-scale evaluation of rock-breaking characteristics.

Limestone, a sedimentary rock composed predominantly of calcium carbonate, offers a suitable candidate for laser-based processing due to its moderate strength, thermal sensitivity, near homogeneous chemical structure, and industrial relevance in mining and geothermal applications [30]. It is found to undergo considerable mass loss during laser-induced heating, which occurs due to partial thermal decomposition of dolomite (CaMg(CO₃)₂) and calcite (CaO), a

major constituent of limestone [31]. Considering its abundance in lithological compositions across the globe, understanding the influence of laser parameters on its mechanical characteristics, such as hardness, is essential for optimizing laser-assisted excavation strategies.

This study examines the effect of key laser processing parameters, viz., laser power, scanning speed, scan line interval, and stand-off distance, on limestone. A general full factorial approach is employed to conduct 81 experiment sets for different combinations of these parameters, and the performance of laser interaction is evaluated through the metric, Rockwell hardness (HRA), which is a micro-indentation-based hardness testing method. To reduce redundancy and the impact of anisotropy, discs of limestone are selected considering its high calcium carbonate concentration and predictable thermal decomposition mechanism. Additionally, it resonates a near homogeneous chemical composition with high content of carbonate, which makes the analysis more standardized. The parametric dependency and influences are discussed in detail in the results and discussion section, which also consists of an analysis of the extent of the laseraffected zone and the possibility of its interference in the evaluation metrics. The aim is to understand relationships between processing parameters and rock weakening, assess the feasibility of utilizing Rockwell hardness (HRA) as an indicator of rock's weakening during laser interaction, and contribute to the process parameter selection, optimization, and design of efficient laser-integrated rock breaking sys-

2. Materials and Methods

The specimen investigated in this study was the limestone rock procured from the Sohra region in the East Khasi hills of Meghalaya, India. It was subsequently sized into standard NX-sized disc cores of 54 mm diameter and 27 mm height (Figure 1). These core samples were prepared using a diamond-tipped coring drill and subsequently cut and polished to achieve flat and parallel surfaces on both ends to ensure uniform laser interaction and testing. The surfaces were further cleaned using compressed air and ethanol to remove any debris or moisture prior to laser irradiation. All the samples were stored under the laboratory conditions (22-25 °C; relative humidity: 40-50%) to minimize environmental influence. Three core samples are utilized in the current investigation for conducting three sets of 27 experiments at three stand-off distances (6, 7, and 8 mm) for various combinations of laser power, scanning speed, and scan line interval, each at three levels. The values of input parameters used are: laser power (126, 144, and 162 W), scanning speed (30, 40, and 50 mm/s), and scan line interval (0.1, 0.2, and 0.3 mm). A general full factorial design approach is utilized for the 81 experimental runs, and the samples are interacted with a 180 W capacity continuous wave CO2 laser with a focal length of 50.8 mm, and a coolant air pressure of 0.3 MPa. Subsequently, after the interaction, each of the samples is analyzed under a digital Rockwell hardness tester (Make: FIE) at 100 kgf load using M-type 1/4" steel ball indenter with 130 display. The samples are also analysed for microstructural alterations and the laser-affected zone. The analysis of the laser-affected zone is performed through Optical microscopy (Make: Carl Zeiss, Model: SMZ25 Nikon StereoZoom Microscope) and ImageJ software, while the microstructural analysis is carried out through Field Emission Scanning Electron Microscopy (FESEM) (Make: Zeiss; Model: Sigma 300). The average initial hardness of the pristine limestone samples

was 122.4 ± 0.9 HRA, with an arithmetic mean roughness (R_a) of 9.82 μ m.

instructions, the beam is emitted through the output window and first directed by a series of high-reflectivity mirrors. These mirrors direct the beam trajectory vertically downward towards the focusing lens, and further to the target material.

The focusing lens converges the collimated laser beam

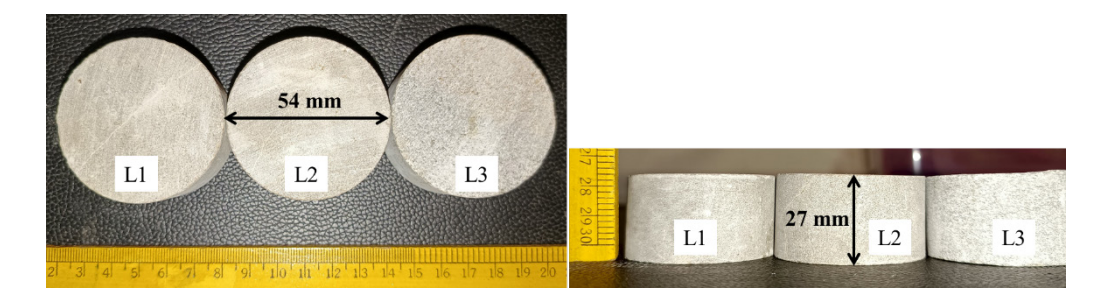


Fig. 1 Dimensions of the disc specimens: Limestone.

A continuous wave CO₂ laser was selected owing to its ability to cause gradual thermal weakening with consistent delivery of thermal energy over the exposure time. This is beneficial in inducing weakening in geological materials. While pulsed lasers are effective in material ablation, they often lead to localized spallation or explosive fragmentation, which can complicate hardness testing measurements.

A schematic of the CO₂ laser system used for the experiment on limestone samples is illustrated in Figure 2. The

onto a small spot defined by the spot diameter on the surface of the rock sample. This spot diameter (\emptyset_{spot}) is governed by the focal length and the stand-off distance. The setup additionally employs a chiller unit for maintaining a stable operating temperature, while preventing overheating, and an air compressor to blow air near the nozzle, assisting in the removal of the debris and cooling the interaction zone. Figure 2(a) illustrates the components of the laser beam delivery system.

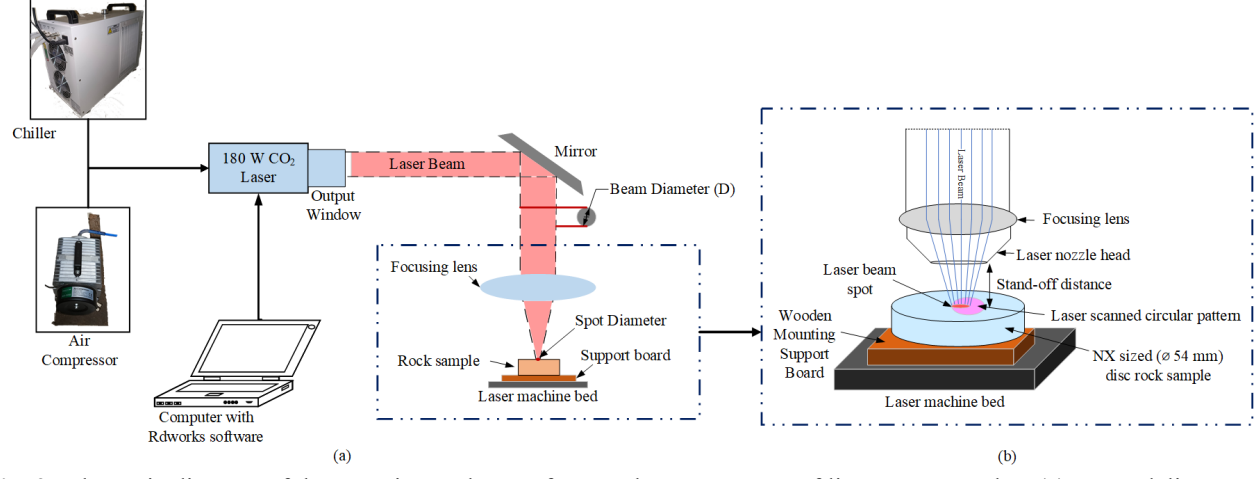


Fig. 2 Schematic diagram of the experimental setup for CO₂ laser treatment of limestone samples: (a) Laser-delivery and control system with focusing optics: (b) Close-up view of rock sample mounting and laser interaction zone showing beam focusing, stand-off distance, and scan pattern.

experimental configuration comprises two primary subsystems: the Laser beam delivery system and the sample positioning setup.

(a) Laser beam delivery system

Laser source employed in this study was a continuous-wave (CW) CO_2 laser having a maximum power capacity of 180 W and a wavelength of 10.6 μ m. The system consists of a laser tube, a mirror, a laser machine bed, a mounting support, a focusing lens, and a dedicated computer with RDworks software. RDworks software is the controlling interface for the laser-material interaction. As per the fed

(b) Rock sample positioning and exposure

The rock samples are prepared as disc specimens of standard NX size (54 mm diameter and 27 mm height). The Samples are mounted on a support to ensure stability during the laser treatment. The beam impinges vertically onto the surface of the disc sample and is used to scan a circular pattern of 2 mm diameter through raster scanning mode, thereby uniformly covering the desired area. The stand-off distance is measured using a calibrated stepped instrument, and the laser nozzle head is positioned perpendicular to the sample head. Further, laser scanning is executed through the software-defined dimensions, allowing for repeatability and

precise manipulation of parameters such as power, scanning speed, and scan-line interval. The schematic for a magnified view of rock mounting and laser interaction is shown in Figure 2(b).

The selection of process parameters for the laser-rock interaction in this study was based on literature trends, machine constraints, and preliminary trials to ensure effective thermal ablation without excessive fracturing, surface melt-

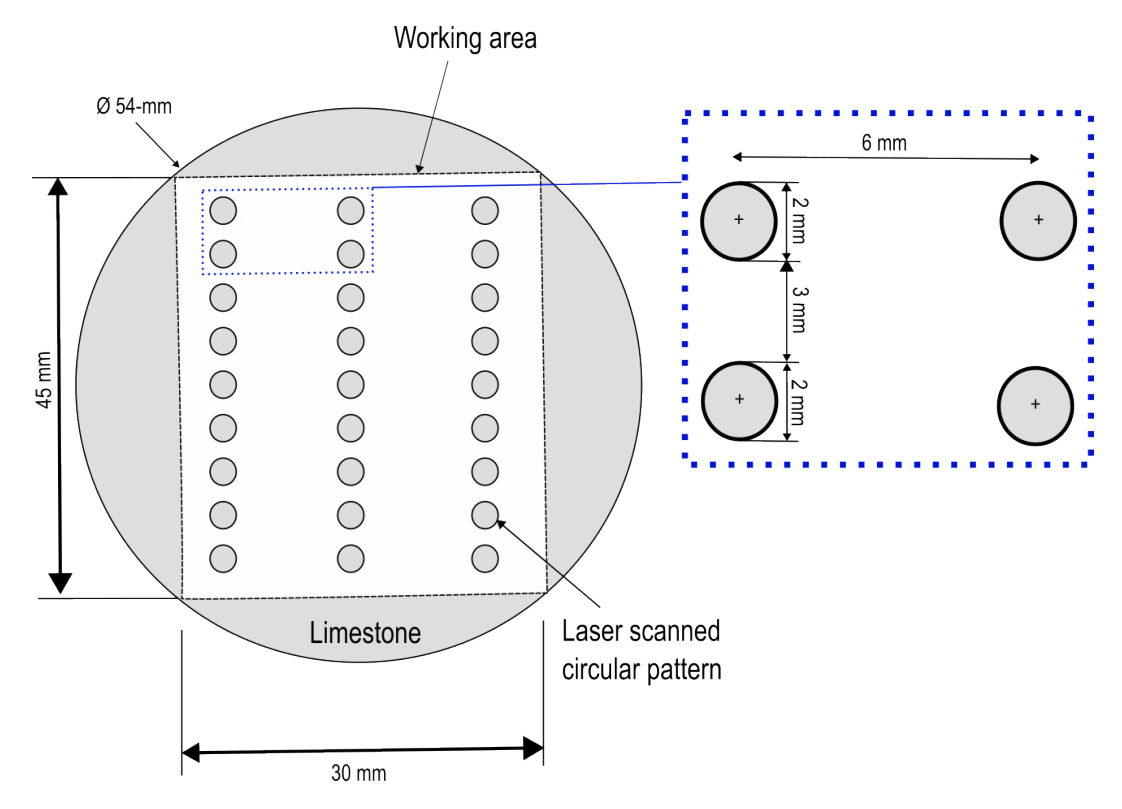


Fig. 3 Schematic representation of the experimental layout on a 54 mm diameter limestone disc. Laser-scanned circular patterns were arranged in a rectangular grid across the working area, with spacing optimized to ensure thermal independence and accurate spatial control. The inset shows a magnified view of the sub-array with defined inter-spot distances

The experimental scheme designed for this study is presented in Figure 3. The 54 mm diameter samples were measured for a defined rectangular working area of 45 mm × 30 mm. A series of laser-scanned circular holes of 2 mm diameter were created using laser beam exposure. Each of the circular spots corresponded to a single experimental condition defined by varying the parameters such as laser power, scanning speed, stand-off distance, and scan diameter. Magnified view in the inset of Figure 3 highlights the precise spatial arrangements of the circular laser patterns. Each circular pattern had 5 mm spacing between the centers vertically and 6 mm spacing in the x-direction. The spacings were calculated in a way that maintained regularity in the study and standardized the observations. The total sub-array spanned 6 mm between the two circles, enabling dense yet non-overlapping exposure to maximize sample usage and ensure thermal isolation between the spots. This experimental scheme ensured systematic variation of parameters across the spots, minimized thermal interaction between adjacent scans, made mechanical testing post-experiments (Rockwell hardness) easier, and ensured consistent and repeatable data acquisition over multiple trials. Computer-controlled motion of the laser through RDworks software helped in the careful positioning of these circular patterns to maintain precision in location, depth, and diameter of the interaction.

ing, pulverization, and debris amalgamation. The four key process parameters considered were laser power (P), standoff distance (SOD), scanning speed (s), and scan interval (s_l). Three levels of these parameters are considered in the general full factorial design as presented in Table 1. The spot diameters measured against the corresponding SODs are also presented in Table 1. Laser power was varied at 126 W, 144 W, and 162 W to investigate the influence of thermal energy input on the mechanical strength of the rock. Standoff distance, described as the vertical gap between the laser nozzle head and the rock surface, was used as 6 mm, 7 mm, and 8 mm, affecting the beam spot size and intensity distribution. Scanning speed was varied at 30 mm/s, 40 mm/s, and 50 mm/s to examine the impact of the energy exposure duration and thermal diffusion. Lastly, the scan line interval, defined as the pitch between the consecutive scan lines during raster scanning of circular patterning, was controlled at 0.1 mm, 0.2 mm, and 0.3 mm to analyze the effect on surface coverage density and thermal overlap. Through this full factorial approach, a comprehensive evaluation of both the individual and interactive effects of these parameters is analyzed on the rock mechanical properties, such as Rockwell hardness (HRA). This contributes to a deeper understanding of the laser-assisted rock weakening mechanism through the context of using Rockwell hardness as an indicator of the rock's strength.

Table 1 Process parameters and their levels for full factorial experimental design in CO₂ laser treatment of limestone samples.

Parameters	I	II	III
Laser power (W)	126	144	162
Stand-off distance (mm)	6	7	8
Spot diameter (Øspot)	0.1	0.25	0.4
Scanning speed (mm/s)	30	40	50
Scan interval (mm)	0.1	0.2	0.3

3. Results and Discussion

The influence of laser processing on the mechanical integrity of the limestone was investigated through a systematic full factorial experimentation as presented in Figures 4 and 6. The softening behavior of the limestone samples under laser irradiation was evaluated through five replicates of experimental runs for laser scanning of circular patterns. The metric used for evaluation of softening behavior was Rockwell hardness (HRA). The experimental setup for the evaluation is illustrated in Figure 5. The results were statistically analyzed to compute mean hardness (HRA_{m}), standard deviation (HRA_{sd}), variance (HRA_{var}), and standard error (HRA_{err}) for the values of the Rockwell Hardness. The results are presented in Figures 7 and 8, and the complete data are provided in Table 2 as the supplementary material.

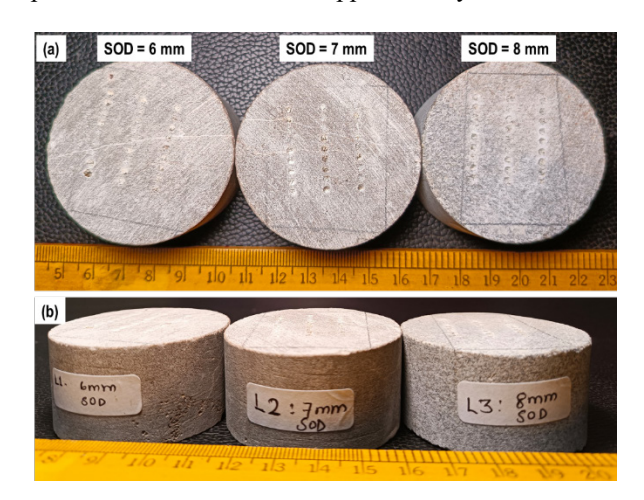


Fig. 4 Macroscopic visual observation of laser irradiated limestone samples at the three stand-off distances (SODs) (a) top view; (b) side view.

Figure 6 reveals distinct morphological transitions across the test matrix, strongly influenced by the local thermal field and laser-material coupling efficiency. The laser-affected zones exhibit increasingly diffused and irregular ablation boundaries with increasing stand-off distances. At 6 mm SOD (Figure 6(a)), the ablation zones appear well-defined, with sharper boundaries and pronounced melt-resolidification rims surrounding the indentations – indicative of localized, high thermal gradients. In contrast, the morphology at 7 mm SOD (Figure 6(b)) displays slight peripheral darkening and uneven surface topography, suggesting lateral heat conduction extending beyond the nominal beam

diameter. At 8 mm SOD (Figure 6(c)), the irradiated spots appear broader and less sharply bounded, which is consistent with increased beam divergence and a wider heat-affected envelope due to defocusing.



Fig. 5 Digital hardness testing setup with a magnified inset of the HRA measurement.

The laser-induced reduction in Rockwell hardness varied distinctly across the three stand-off distances (SOD). The variations were observed to be marginal, though in all three cases, with a few outlier values. For the SOD = 6 mm group, the pre-irradiation mean hardness in the pristine condition for the limestone sample was 121.8 ± 0.36 HRA. For laser-irradiated samples, the mean hardness ranged from 107.04 to 242.44 HRA. While most values exhibited a moderate reduction (HRA_m : 116-120), two runs (Exp. 7 and 8) showed anomalously high hardness values exceeding 230 HRA, likely due to measurement error or recrystallization effects. Excluding these outliers, the average reduction in HRA was approximately 3-5 points from baseline, with the lowest values appearing at higher laser power and lower scan line intervals.

For SOD = 7 mm, the mean initial hardness value was 122.4 ± 0.67 HRA. Post-processing means values ranged between 114.53 and 121.06, indicating relatively limited reduction. The hardness values remained between 1-6% of the original, suggesting lower thermal penetration. This may be attributed to greater beam divergence and reduced energy density at increased SOD, which aligns with the lower severity of microcrack formation observed in FESEM studies.

In contrast, for SOD = 8 mm, the baseline pristine condition mean HRA was 121.2 ± 0.44 . The observed hardness varied widely from 114.54 to 123.34. Although the mean reduction was modest (typically 1-4 points), a few conditions – especially lower scan speed (30 mm/s) with higher power – showed higher softening. This suggests that longer interaction time partially compensated for the laser beam spread at this standoff.

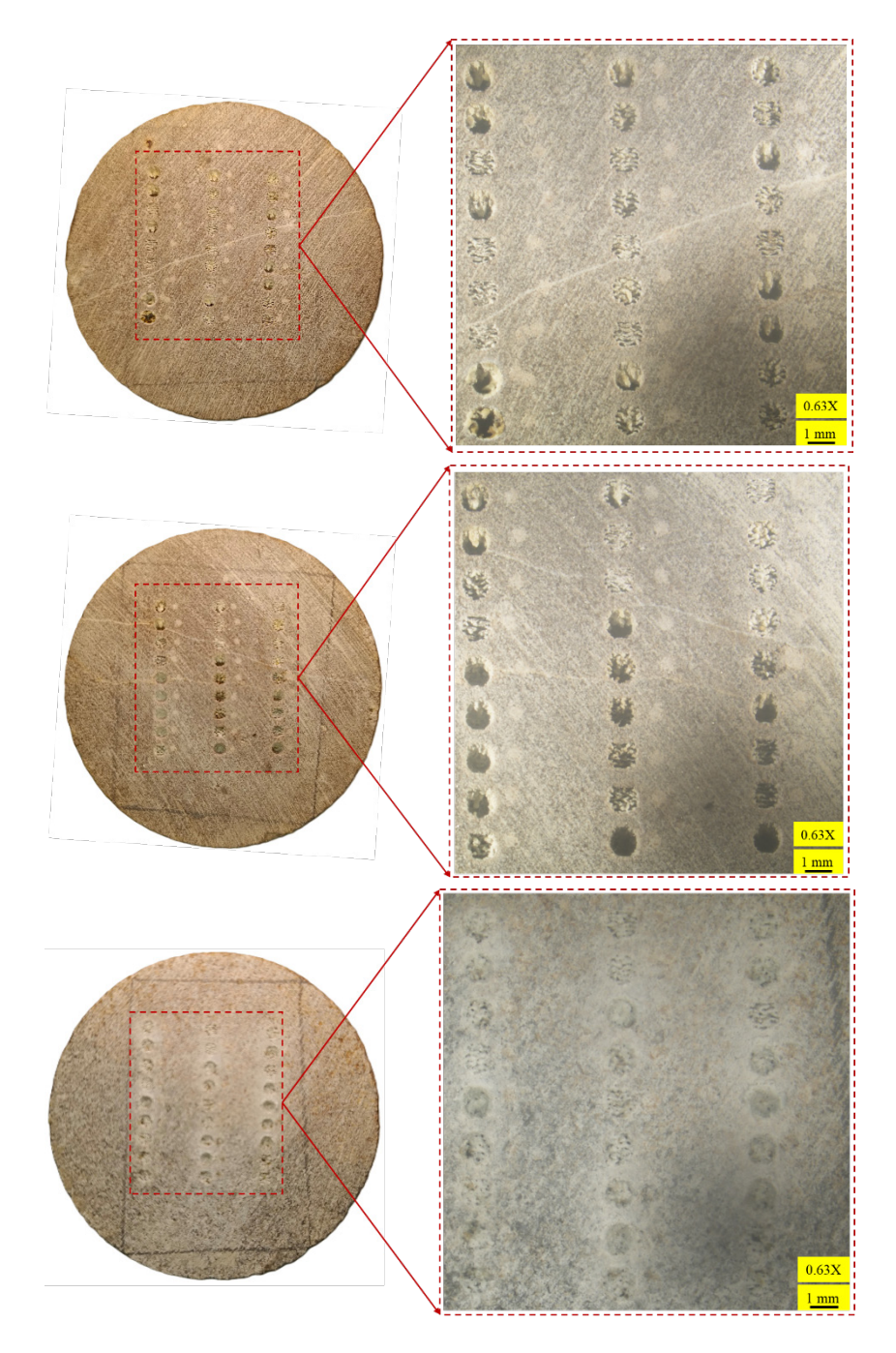


Fig. 6 Surface morphology of Laser-irradiated limestone at (a) SOD = 6 mm, (b) SOD = 7 mm, (c) SOD = 8 mm.

The common morphological stages observed in all three sets of experiments at three SODs are presented in Figure 7. At lower power, higher scanning speed, and higher values of scan line interval, the first stage of the processing, i.e., shallow linear threads, is observed due to the lower energy deposition during the raster scanning. Further, for the combination of mid-power range, higher scan speed, and mid-range scan line intervals, smearing of material and pulverization is observed. A clean hole and complete vaporization are morphologically seen at higher power, low scan speed, and tighter scan line interval. The blurriness in the image occurs in Figures 7(c) and (d) due to defocusing in the removed material zone.

Figure 8 illustrates the box plot distribution of Rockwell hardness (HRA) values across different settings of laser power, scanning speed, and scan-line interval. Figure 8(a) presents it at different laser powers. It is observed that for each SOD level, a consistent trend emerges where higher laser power (162 W) tends to result in slightly lower median HRA values, reflecting enhanced thermal softening effects.

At SOD = 6 mm, the spread in HRA is notably larger, with the visible outliers especially at 144 W and 162 W, indicating localized variations in thermal absorption or possible recrystallization effects. At SOD = 7 mm, hardness values show minimal spread and a tighter interquartile standoff. In contrast, at SOD = 8 mm, the box plots reflect

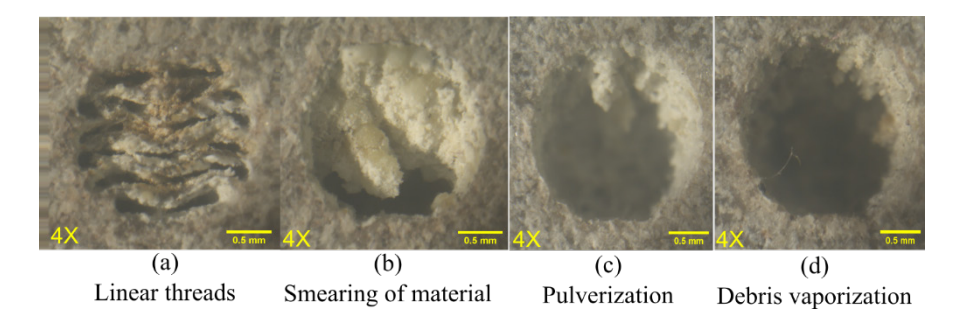


Fig. 7 Common morphological stages observed during laser scanning of the limestone.

slightly broader distributions again, with reduced hardness values consistent with increased laser interaction time due to reduced energy concentration. Interestingly, 126 W at SOD = 7 mm shows almost no variation, implying highly stable processing under those parameters. The presence of outliers in multiple groups underscores the importance of accounting for microstructural heterogeneity and potential inconsistencies in energy coupling due to beam – material dynamics. Overall, it is seen from the box plot that laser power

and stand-off distance significantly influence post-irradiation surface hardness, with thermal softening becoming more pronounced at higher powers and shorter SODs. A box plot illustrating the comparison of Rockwell hardness (HRA) as a function of scanning speed and stand-off distance is presented in Figure 8(b). A distinct trend is observed where lower scanning speeds (30 mm/s) are consistently associated with marginally reduced HRA values across all SOD levels, indicating more effective laser-induced

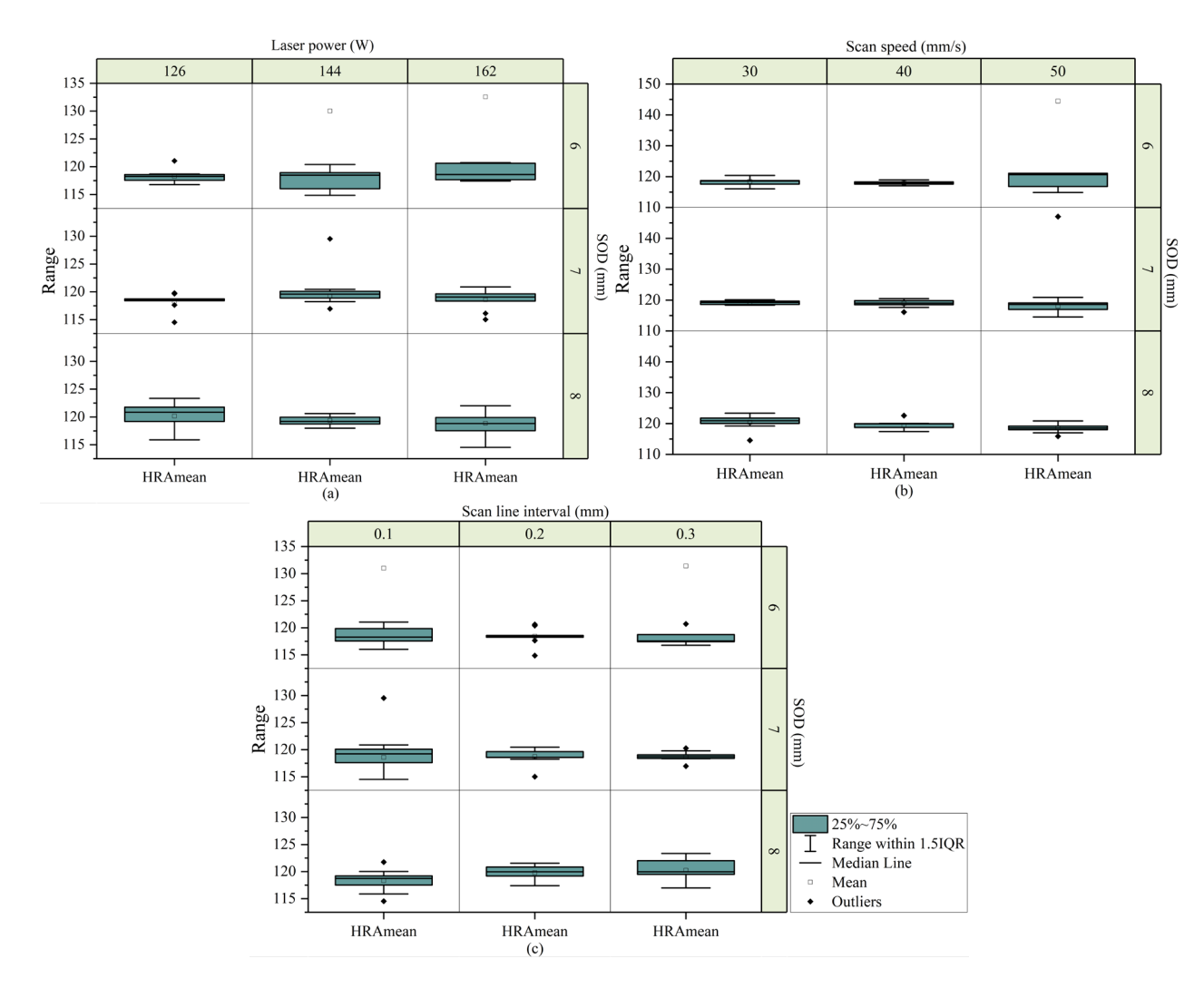


Fig. 8 Illustration of box-plot trend for Rockwell hardness (HRA) against (a) Laser power, (b) Scanning speed, and (c) Scan line interval at three Stand-off distances (6, 7, and 8 mm).

softening. This can be attributed to the longer interaction time per unit area at lower scan speeds, which facilitates deeper thermal penetration and microstructural damage. At higher scan speeds (50 mm/s), the hardness tends to remain higher and displays increased variability, especially at SOD = 6 mm, where a notable outlier corresponds to abnormally high HRA – potentially due to insufficient heat accumulation or anomalous surface recrystallization. At SOD = 7 mm and 8 mm, the HRA medians across all scan speeds cluster closely, suggesting the effect of increased beam divergence and reduced thermal concentration at higher SODs. Moreover, the 25-76% interquartile range narrows significantly at lower scan speeds for SOD = 7 mm and 8 mm, indicating more uniform laser-material interaction under these conditions. Collectively, the box-plot reinforces the inverse relationship between scan speed and thermal softening, while also emphasizing the nuanced interaction between scanning dynamics and beam focusing effects dictated by stand-off distances. The distribution of Rockwell hardness (HRA) as influenced by scan-line interval across the three SOD values is presented in Figure 8(c). A general trend emerges wherein the smallest scan-line interval (0.1 mm) consistently results in lower median HRA

values, indicating greater material softening. This behavior is attributed to higher thermal accumulation due to increased overlap of adjacent laser passes, which enhances energy input per unit area and promotes deeper subsurface damage. Conversely, larger scan-line intervals (0.2 mm and 0.3 mm) demonstrate higher HRA medians, reflecting less effective thermal coupling and incomplete coverage. At SOD = 6 mm, the effect is most prominent, with tight clustering around the median and noticeable outliers – indicating potential heterogeneities or microstructural instabilities induced by localized overheating. At greater SODs (7 mm and 8 mm), the variability across scan-line intervals is subdued, and distributions narrow, suggesting reduced sensitivity to scan-line spacing due to beam divergence and lower surface energy density. The plot in entirety confirms that smaller scan-line intervals facilitate more effective softening, particularly at lower SOD, reinforcing their importance in laser-induced weakening strategies for geological materials. The analysis from the box plot distribution is supported by the column plots in Figure 9, where not much variation is observed in the HRA values except for a few outliers at SOD = 6 mm.

3.1 Parametric Sensitivity

Laser power: Higher power settings (162 W) were generally associated with increased softening when combined with smaller scan line intervals and slower scan speeds. For

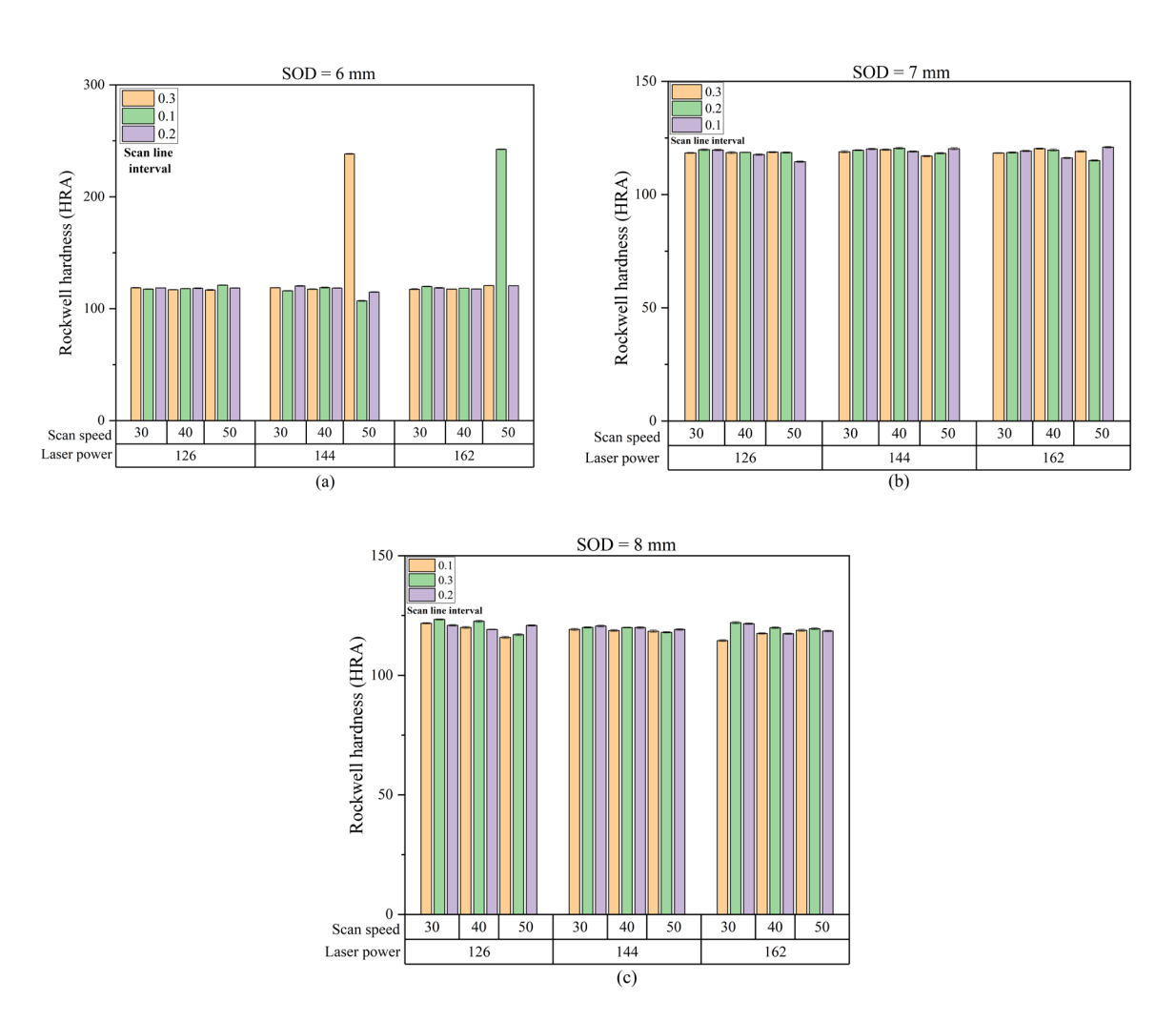


Fig. 9 Rockwell hardness (HRA) trend against varying laser power, scan speed, and scan line interval at different SOD values of (a) 6 mm, (b) 7 mm, and (c) 8 mm.

instance, Exp. No. 2 (P = 162 W, $s_l = 0.1 \text{ mm}$) recorded a mean HRA of 119.86, slightly below the baseline, whereas Exp. No. 20 (P = 162 W, $s_l = 0.3 \text{ mm}$) recorded 117.44. This trend indicates thermal accumulation effects at tighter scanning configurations.

Scan Speed: Low scanning speed (30 mm/s) was consistently correlated with greater softening. At slow scan speeds, beam dwell time increases, allowing deeper thermal diffusion and microstructural damage. For example, Exp. No. 1 (s = 30 mm/s) showed significant hardness reduction compared to Exp. No. 5 (s = 50 mm/s).

Scan line interval: A narrower scan line interval (0.1 mm) enhanced the overlap of the adjacent laser passes, increasing the effective energy input and the heat-affected area. The lowest HRA values often occurred at 0.1 mm intervals. For instance, Exp. 21 ($s_l = 0.1$ mm, P = 144 W, s = 50 mm/s) resulted in $HRA_m = 107.04$, a substantial drop from the baseline pristine condition value.

Statistical deviations ranged from 0.20 to 1.01, suggesting good measurement consistency in most cases. The average HRA error margin across all the experiments remained below \pm 0.5, validating the reliability of the five experimental replications. Experiments involving higher laser power and slower scanning speed exhibited higher variance, likely due to thermal instability and localized melting.

material interaction spot and is a critical indicator of subsurface thermal effects that potentially influence the mechanical integrity of the rock. Figure 10(a-c) depicts the variation in HAZ dimensions across all the 81 experimental runs for three distinct stand-off distances (SODs): 6 mm, 7 mm, and 8 mm.

At SOD = 6 mm, the HAZ predominantly remains below 2.7 mm across all input combinations. Notably, a slight increase in HAZ is observed at lower scan speeds and higher laser powers, which is consistent with the longer laser-rock interaction time and greater thermal flux. Among the scanline intervals, the 0.1 mm setting exhibits slightly higher HAZ values, particularly at 162 W and 30 mm/s, indicating enhanced thermal accumulation due to closer pass overlaps.

With SOD = 7 mm, the HAZ values stabilize around a similar range as those at 6 mm, albeit with reduced peak variations. This trend suggests a relatively optimized beam focusing at this distance, where thermal diffusion is more localized, and excess heating is minimized. The marginal decrease in HAZ with increasing scan speed is again evident, indicating that laser traversal limits the radial spread of the heat.

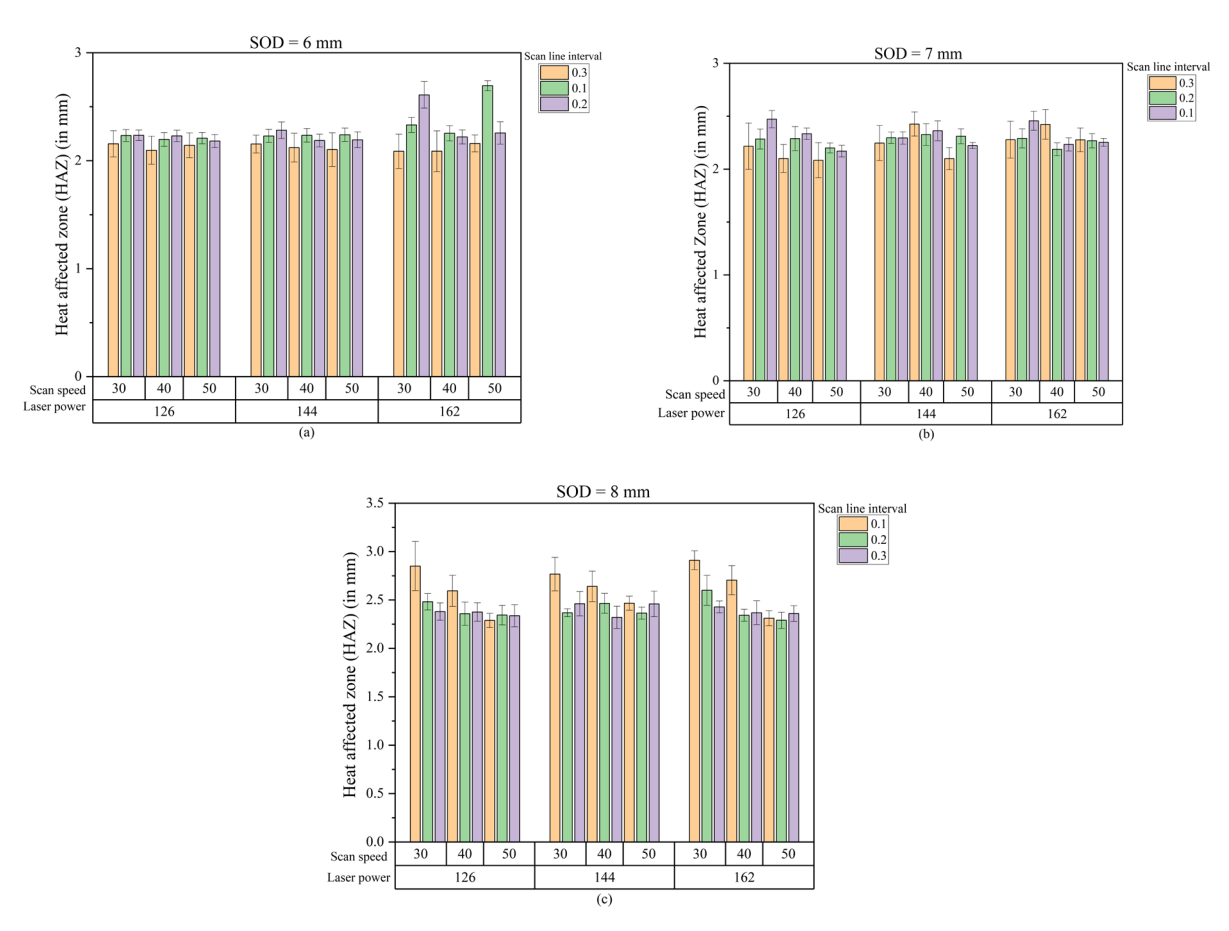


Fig. 10 Heat-affected zone (in mm) plotted against the laser power, scan speed, and scan line interval at the three SOD values of (a) 6 mm, (b) 7 mm, (c) 8 mm.

3.2 Analysis of heat-affected zone (HAZ)

The heat-affected zone (HAZ) in laser-irradiated rocks represents the extent of thermal diffusion beyond the laser-

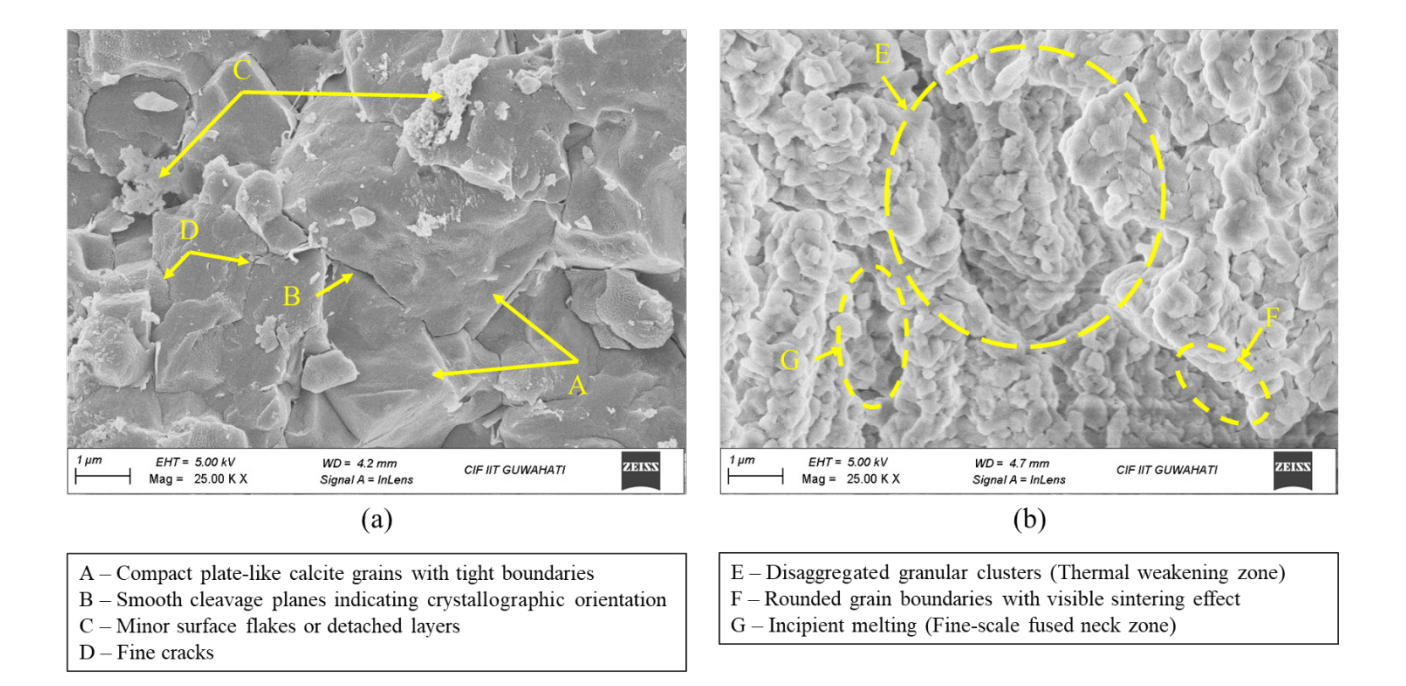


Fig. 11 Field emission scanning electron microscopy (FESEM) images (at 25K X magnification and 1 μm scale) of (a) pristine limestone sample, and (b) laser-irradiated limestone.

At SOD = 8 mm, a noticeable increase in HAZ is observed, with peak values exceeding 3 mm in isolated combinations (e.g., 126 W, 30 mm/s, and 0.1 mm interval). This is attributed to beam defocusing at larger SODs, which results in a wider but less intense energy distribution, increasing the surface area affected by heat. Importantly, this broader beam diameter at 8 mm SOD leads to a more significant HAZ due to thermal smearing, although the laser fluence is effectively lower

It is observed that in all the cases, HAZ values predominantly remain below 3 mm, except in a few cases of 8 mm SOD. The effective beam footprint for scanning the circular pattern of 2 mm goes only up to 1-1.2 mm beyond 2 mm, which is quite below the 3 mm inter-spot spacing between each circular scan as per the proposed experimental design. Hence, this minimizes the thermal interference during the analysis and aids in effectively evaluating the Rockwell hardness. Through the presented experimental design and the HAZ evaluation, it is observed that the individual irradiation zones were thermally insulated from their neighboring zones under all the experimental combinations. Though spatial overlap was effectively avoided, minor anomalies in hardness trends can be attributed to material anisotropy or localized cumulative heating effects.

Additionally, the higher spread in the HAZ at 8 mm SOD, with reduced hardness even in the presence of potential oxide, suggested that the thermal degradation, microfracturing, and possible decomposition of carbonate phases (dolomite and calcite) likely dominate over any surface hardening effects from oxides.

3.3 Microstructural analysis

A high-resolution field emission scanning electron microscopy (FESEM) of the pristine limestone surface is presented in Figure 11(a). The sample was imaged under a

working distance of 4.2 mm to assess the baseline microstructural morphology prior to laser exposure. The mean Rockwell hardness values of the analyzed pristine limestone sample was 122.4 ± 0.9 HRA.

A compact arrangement of platy and angular micritic grains can be clearly seen, which is the characteristic of sedimentary carbonates predominantly composed of calcite (CaCO₃). The grains exhibit a polygonal morphology with relatively smooth surfaces and clean intergranular boundaries, suggesting a tight mineralogical packing. The absence of significant inter-crystalline voids or microcracks indicates that the limestone sample retained its natural compactness and mechanical integrity prior to irradiation. This observation can be correlated with the high mean Rockwell hardness values recorded for unprocessed samples (121.8 to 122.4 HRA), supporting the mechanical uniformity of the pristine matrix.

A few fine intergranular gaps and minor detached flakes are observed, possibly due to sample preparation effects such as polishing or handling. However, these features are sparse and isolated, confirming the homogeneity of the untreated surface. The lamellar texture and smooth cleavage planes suggest a calcitic dominance with minimal structural defects, which is expected in a non-porous crystalline limestone sample.

Figure 11(b) illustrates the FESEM image for the laser-irradiated limestone sample. In contrast to the pristine sample, this image reveals a drastically altered microstructure with evidence of thermal decomposition, localized melting, and crack initiation. The grains have lost their sharp polygonal edges and appear rounded, disaggregated, and sintered, forming cauliflower-like micro textures — a signature of high-temperature exposure and partial surface vitrification. The laser-induced temperature gradients likely exceeded the thermal decomposition threshold of CaCO₃, leading to

micro-spallation, pore coalescence, and localized detachment of the particulates.

These morphological transformations indicate severe microstructural degradation due to thermal stress accumulation, which weakens intergranular cohesion and promotes grain boundary decohesion. The absence of large-scale cracks and instead, the presence of widespread micro-fractures and surface roughening reflect a subsurface weakening mechanism, corroborating with the observed reduction in Rockwell hardness (HRA) values in laser-treated samples – often dropping by 2-5 points depending on input parameters.

The fine-scale particle agglomeration and fusion necks between grains further suggest localized melting-recrystallization cycles, which are consistent with the observed thermal damage zones in macroscopic sample inspections. Such thermal-induced textural evolution supports the hypothesis that laser interaction leads to progressive mineral weakening via microcrack initiation and surface restructuring.

The pristine condition microstructure provides a reference for assessing laser-induced damage mechanisms. The uniform grain packing, absence of fracture networks, and minimal porosity establish the foundational mechanical strength observed in the initial hardness values. Subsequent comparison with the post-irradiated images reveals the extent of microcrack development, thermal degradation, and grain boundary decohesion induced by laser interaction. The transformation from smooth, crystalline grains to fractured, irregular morphologies in the irradiated zones can be directly attributed to the thermal shock and localized expansion generated by laser heating, which is substantiated by both microstructural evidence and the mechanical property degradation.

The mechanical changes observed through the microstructure of the laser-exposed limestone explain the significant softening trends seen in Rockwell hardness after laser irradiation. The disrupted grain structure reduces the material's ability to resist indentation, thereby validating the mechanical degradation trends observed in the parametric study. Furthermore, the absence of visible long cracks aligns with the hypothesis that damage accumulation in laser-treated limestone is gradual, diffuse, and thermally driven rather than impact or shock-induced.

4. Conclusion

This study systematically investigated the softening behavior of limestone under laser irradiation using Rockwell hardness (HRA) as a primary indicator of the mechanical degradation. The key conclusions deduced are as follows:

- The degree of hardness reduction was significantly influenced by stand-off distance (SOD), with closer distances (6 mm) showing pronounced softening due to higher energy density and thermal penetration, while greater distances (7 mm and 8 mm) showed reduced softening effects owing to beam divergence and lower energy coupling. Some anomalies were observed due to possible recrystallization or local thermal effects
- 2. Parametric analysis reveals that:
 - a. Higher power (162 W), particularly when paired with lower scan line intervals (0.1 mm) and slower scanning speeds (30 mm/s),

- produced greater softening effects due to thermal accumulation
- Lower scan speeds facilitated longer beam interaction time, increasing the heat input and depth of microstructural alteration
- c. Narrow scan line intervals enhanced overlap and energy concentration, leading to more extensive thermal damage and reduced hardness
- 3. Statistical evaluation revealed low standard errors ($< \pm 0.5$ HRA) in most cases, confirming good repeatability. Experiments with higher thermal input exhibited increased variance, likely due to non-uniform melting and thermal instability.
- Analysis of the heat-affected zone (HAZ) confirms that the thermal diffusion remains confined below
 mm throughout the experimentation, avoiding thermal overlap or cumulative heating effects during the laser scanning experiments.
- 5. FESEM analysis demonstrates a clear contrast between pristine and irradiated microstructures, where laser exposure caused grain boundary decohesion, surface vitrification, micro-fracturing, and sintering, all indicative of laser-induced thermal degradation and consistent with the observed mechanical weakening.

These findings confirm a strong correlation between laser parameters, microstructural transformation, and mechanical softening, emphasizing the potential for controlled laserrock interaction to facilitate targeted weakening in applications such as thermal-assisted rock drilling and mineral processing. Chemical analysis integrated with the geo-mechanical approach presented in the current study can further aid in a deeper understanding of the laser-based rock softening.

Acknowledgement

This work is supported by IITG Technology Innovation and Development Foundation (IITGTI&DF), which has been set up at IIT Guwahati as a part of the National Mission on Interdisciplinary Cyber-Physical Systems (NMICPS), IITGTI&DF is undertaking the financial assistance from the Department of Science and Technology, India, through grant number DST/NMICPS/TIH12/IITG/2020. The authors gratefully acknowledge the support provided for the present work.

References

- [1] A. Gowida, H. Gamal, and S. Elkatatny: Geoenergy Sci. Eng., 230, (2023) 212278.
- [2] R. M. Graves, A. A. Ionin, Y. M. Klimachev, A. F. Mukhammedgalieva, D. G. O'Brien, D. V. Sinitsyn, and V. D. Zvorykin: Proc. SPIE, Vol. 4065, (2000) 602.
- [3] A.K. Sinha and S.N. Joshi: "Low cost Manufacturing Technologies" ed. by S.N. Joshi, U.S. Dixit, R.K. Mittal, S. Bag, (Springer, Singapore, 2023) 3.
- [4] E. Rossi, S. Jamal, V. Wittig, M. O. Saar, and P. R. von Rohr: Geothermics, 85, (2020) 101771.
- [5] M. A. Kant, E. Rossi, C. Madonna, D. Höser, and P. Rudolf von Rohr: J. Geophys. Res. Solid Earth, 122, (2017) 1805.

- [6] R. A. Parker, B. C. Gahan, R. M. Graves, S. Batarseh, Z. Xu, and C. B. Reed: Proc. SPE Annu. Tech. Conf. Exhib., (2003) SPE-84353-MS.
- [7] P. Sinha and A. Gour: Proc. SPE/IADC Indian Drill. Technol. Conf. Exhib., (2006) SPE-102017-MS.
- [8] Z. Xu, C. B. Reed, G. Konercki, R. A. Parker, B. C. Gahan, S. Batarseh, R. M. Graves, H. Figueroa, and N. Skinner: J. laser applications, 15, (2003) 25.
- [9] B.C. Gahan, R.A. Parker, S. Batarseh, H. Figueroa, C. B. Reed, and Z. Xu: Proc. SPE Annu. Tech. Conf. Exhib., (2001) SPE-71466-MS.
- [10] Z. Xu, C.B. Reed, R.A. Parker, B.C. Gahan, R.M. Graves, and H. Figueroa: Proc. ICALEO, 21st Int. Congr. Laser Mater. Process. Laser Microfabrication, (2002) 160291.
- [11]B. C. Gahan, R.A. Parker, R. Graves, S. Batarseh, C.B. Reed, Z. Xu, H. Figueroa, and N. Skinner: Gas Technology Institute Report, Des Plaines, IL(USA), (2001).
- [12] K. Fu, Q. Li, S. Fu, Z. Huang, K. Chen, Y. Hou, and J. Li: Geoenergy Sci. Eng., 241, (2024) 213090.
- [13] A. Riveiro, A. Mejias, R. Soto, F. Quintero, J. del Val, M. Boutinguiza, F. Lusquiños, J. Pardo, and J. Pou: Opt. Laser Technol., 76, (2016) 19.
- [14] H. Pan, Y. Hu, Y. Kang, H. Chen, F. Liu, J. Xie, and X. Wang: J. Pet. Sci. Eng., 213, (2022) 110397.
- [15] H. Pan, Y. Hu, Y. Kang, Z.F. Wang, J.W. Liu, H. Chen, and M.D. Zhang: Pet. Sci., 19, (2022) 2969.
- [16] K. Chen, Z. Huang, R. Deng, W. Zhang, M. Kang, and Y. Ma: Rock Mech. Rock Eng., 55, (2020) 2129.
- [17] F. Rui and G. F. Zhao: Int. J. Rock Mech. Min. Sci., 139, (2021) 104653.

- [18] A. K. Sinha and S. N. Joshi: J. Micromanuf., 0, (2025) 25165984251319132.
- [19] J. Liu, Y. Xin, W. Lv, Y. Zhu, B. Ren, H. Pan, and Y. Hu: Appl. Sci., 13, (2023) 4347.
- [20] H. Pan, Y. Hu, H. Liu, Y. Guo, Y. Kang, W. Wang, and Y. Liu: Rock Mech. and Rock Eng., 58, (2025) 3437.
- [21] D.P. San-Roman-Alerigi, S.I. Batarseh, and Y. Han: Proc. ARMA US Rock Mech./Geomech. Symp., (2016) ARMA-2016-142.
- [22] J. Dutta Majumdar and I. Manna: Int. Mater. Rev., 56, (2011) 341.
- [23] F. Buckstegge, T. Michel, M. Zimmermann, S. Roth, and M. Schmidt: Phys. Procedia, 83, (2016) 336.
- [24] S. Ghorbani, S. H. Hoseinie, E. Ghasemi, and T. Sherizadeh: Arab. J. Geosci., 15, (2022) 1067.
- [25] S. Gstalder and J. Raynal: J. Pet. Tech., 18, (1996) 991.
- [26] H. Aldeeky, O. Al Hattamleh, and S. Rababah: Mater. Constr., 70, (2020) e230.
- [27] A. Tsikrikis, V. Marinos, and T. Papaliangas: Proc. ISRM Congr., (2023) ISRM-15CONGRESS.
- [28] S.H. Hoseinie, M. Ataei, and R. Mikaiel: Arab J Sci Eng 37, (2012) 1451.
- [29] Y. Wang, G.M. Grammer, G. Eberli, R. Weger, and R. Nygaard: J. Pet. Sci. Eng., 210, (2022) 109973.
- [30] V. Martínez-Ibáñez, M.E. Garrido, C. Hidalgo Signes, A. Basco, T. Miranda, and R. Tomás: Appl. Sci., 11, (2021) 3286.
- [31] H. Pan, Y. Kang, Y. Hu, F. Liu, J. Xu, D. Li, and J. Li: Int. J. Rock Mech. Min. Sci., 174, (2024) 105638.

(Received: June 30, 2025, Accepted: October 10, 2025)